Additive Manufacturing 83 (2024) 104063

Contents lists available at ScienceDirect

Additive Manufacturing

journal homepage: www.elsevier.com/locate/addma

Polypropylene for material extrusion: Evidence that flow-enhanced crystallization restricts welding

Zakarya Baouch [a], Riccardo Vezzoli [a], Jessy Koster [b], Andrea Costanzo [a], Andrea Lanfranchi [a], Dario Cavallo [a,*], Claire McIlroy [c,*]

[a] University of Genoa, Department of Chemistry and Industrial Chemistry, Via Dodecaneso 31, Genova 16146, Italy
[b] Polymer Technology, Department of Mechanical Engineering, Eindhoven University of Technology, P.O. Box 513, Eindhoven 5600 MB, the Netherlands
[c] School of Maths & Physics, University of Lincoln, Lincoln LN6 7TS, United Kingdom

ARTICLE INFO

Keywords:
Material-extrusion
Polypropylene
Welding
Flow-enhanced crystallization

ABSTRACT

We present a comprehensive investigation into the effect that both the crystallization kinetics and the molecular weight of polypropylene feedstock have on the welding properties in material extrusion 3D-printing (MatEx). As sufficient welding at the interfaces between printed layers may be restricted by the onset of crystallization, there is a delicate balance between polymer interdiffusion and the development of spherulites within the weld region. We monitor these processes during a cooling cycle using a well-established theoretical model that requires full characterisation of the rheology and crystallization. The model shows that the largest effect of increasing molecular weight is a reduction in interdiffusion; this mechanism leads to a reduction in the weld strength as demonstrated by mechanical testing. For the highest molecular weight feedstock, we find that the fracture pattern changes from plastic deformation to brittle mode. Furthermore, we observe that the spherulites within the weld are about an order of magnitude smaller than in other samples. These observations cannot be described by the quiescent crystallization kinetics alone. Our findings suggest that it is a flow-enhanced crystallization mechanism that accelerates nucleation leading to smaller spherulites developing in the weld earlier in the cooling process. This significantly restricts interdiffusion at the welds.

1. Introduction

Material extrusion (MatEx) of thermoplastics continues to dominate as the cheapest and most tractable additive manufacturing technology. However, the delicate balance of the hot extrusion flow followed by relatively fast cooling and solidification limits the range of printable materials [1]. For instance, high-performance thermoplastics that are highly desirable for advanced applications (e.g., in aerospace) are often incompatible with the MatEx process as they tend to be semi-crystalline polymers with sharp melting points. These materials contain both amorphous regions and domains of highly ordered and tightly packed chains segments; these areas of crystallinity are organized into spherical aggregates, i.e., spherulites, and enhance strength and durability of thermoplastic products. However, semi-crystalline polymers are notoriously difficult to process using MatEx for several reasons. Here we focus on the challenge of ensuring strength at the interfaces between layers of polypropylene (PP) [2–6].

It is well known that interdiffusion of the polymer molecules across the filament-filament interface is the key to ensuring strength at the welds between layers [7]. In amorphous polymers, this diffusion process is arrested by a glass transition, which in unfavourable conditions can lock in residual alignment and reduce mechanical properties [8–10]. In semi-crystalline polymers, once the temperature drops below the crystallization temperature the polymer will nucleate and spherulites will begin to grow. If the glass transition is below the ambient temperature, as in PP, then crystallization will proceed to full space filling during cooling. It is known that this crystallization process slows down the polymer dynamics [11], with inter-diffusion expected to be arrested once full space filling is achieved [12]. Thus, for semi-crystalline polymers the dominating mechanism restricting welding tends to be the (temperature dependent) crystallization rate, rather than the time above the glass transition. Furthermore, the mechanical properties achieved at solidification depend on the size and volume fraction of the spherulites that develop during crystallization and is therefore inherently linked to the temperature profile. In MatEx, the cyclic heating-cooling profiles induced by the layer-by-layer process makes for a complex thermal

---

* Corresponding authors.
E-mail addresses: dario.cavallo@unige.it (D. Cavallo), CMcilroy@lincoln.ac.uk (C. McIlroy).

https://doi.org/10.1016/j.addma.2024.104063
Received 2 December 2023; Received in revised form 24 February 2024; Accepted 27 February 2024

history [13], which may lead to inhomogeneity in the crystal structure at the microstructural level. Flow can also have significant effects on this spherulite structure; if a polymer experiences flow rates sufficiently strong that stretched chains persist at the onset of nucleation, then nucleation will be accelerated. As well as resulting in smaller and more densely packed spherulites [14], accelerated crystallization has the potential to impede interdiffusion since the effective weld time is reduced.

Flow-enhanced crystallization kinetics under additive manufacturing MatEx conditions has been directly measured in-situ for polycaprolactone, where the half-crystallization times decreases by 50% with increasing printing speed at the lowest extrusion temperature. [15] Moreover, some effect on the printing conditions on the morphology of annealed poly-lactic acid could also be predicted by modelling and captured by ex-situ measurements [16]. However, it is unclear how this mechanism effects welding and the build-up of strength between layers. Flow-induced crystallization is ubiquitous in traditional manufacturing of PP, such as during injection moulding [17], leading to intricate oriented crystal structures called shish kebabs that can enhance mechanical properties. It is expected that flow-enhanced nucleation of PP is also possible under MatEx conditions [18]. In fact, a close inspection of cross-section morphologies of 3D printed specimen available in the literature reveals a gradient of spherulite dimension, with the radius being smaller close to the weld region [2] or even oriented crystalline morphology at the weld [5]. The flow-induced crystalline morphology of PP was shown to be dependent on the printing parameters, with mild conditions (high nozzle temperatures and low printing speed) leading to homogeneous morphology, while pronounced inhomogeneity in the crystalline structure was produced at low extrusion temperatures and high printing speeds [5].

Here we present prime evidence that flow-enhanced nucleation in PP may be a concern and can impede welding leading to reduced mechanical strength. We believe this to be the first comprehensive investigation to study how both crystallization and molecular weight affect welding during MatEx of PP. Furthermore, we show how favourable conditions may be predicted by a simple model of the crystallization time. This model may be readily extended to any semi-crystalline polymer.

2. Materials and experimental methods

2.1. Materials overview

Table 1 presents the main characteristics of the polymers used in this investigation, sourced from Borealis Polyolefine GmbH. We investigate five distinct polypropylene homopolymers (PPH). See Appendix for further results including a random poly(propene-co-ethylene) copolymer (PPC), and a polypropylene homopolymer with the addition of a nucleating agent (PPN).

2.2. Polymer rheology

Rheological analysis was performed using a HR 10 rheometer (TA Instruments, USA) with 25 mm plate-plate geometry. The materials were processed by heating pellets in the plate-plate configuration at 240 ℃, while a metal strip was used to contain the molten material. After 5 minutes, the metal strip was taken out, and the gap distance was adjusted to 1.05 mm. Subsequently, any surplus material was eliminated, and the gap was further reduced to 1 mm. The rheological measurements were carried out in a range of angular frequencies from 100 to 0.1 rad/s. The amplitude strain was set at 2% within the linear viscoelastic range. This procedure was repeated at five distinct temperatures for each material, ranging from 180 to 240 °C. TRIOS software from TA Instruments was utilized for the time-temperature superposition analysis. This data provides rheological master curves ($G^{'}, G^{''}$ vs frequency at some reference temperature), enabling the calculation of the time-temperature superposition shift factors and rheological time scales, as done in previous work [8]. (See Appendix for further details).

2.3. Differential scanning calorimetry

The thermal characterizations were conducted through differential scanning calorimetry (DSC) analysis using a DSC Q20 instrument (Ta Instruments, USA). Samples weight of around 2–5 mg were encapsulated in aluminium pans.

For non-isothermal crystallization and melting runs, the material is initially melted at 230 ℃ for 5 minutes to eliminate any prior thermomechanical effects. Subsequently, the polymer is cooled at a rate of 10 ℃ /min until −20 ℃. It is then reheated at the same rate of 10 ℃/min back up to 230 ℃. Throughout this process, a supply of 50 ml/min nitrogen is maintained to prevent oxidation. Additionally, isothermal crystallization kinetics has been measured, according to the subsequent procedure.

Initially, the material undergoes a melting phase at 230 ℃ for 5 minutes. Subsequently, the material is subjected to a crystallization process at temperature, T_c, until no further crystallization is observed. Excessive time is avoided to prevent annealing effects. Following the crystallization step, the sample is then heated to 230 ℃ to melt the formed crystals. The heating rate is set at 10 ℃/min, and the cooling rate is chosen at 40 ℃/min. Also in this case, a continuous flow of 50 ml/min of nitrogen is supplied to prevent oxidation. The range of viable crystallization temperatures is influenced by both the cooling speed and the signal resolution, hence the specific temperatures for reliable isothermal crystallization kinetics results vary depending on the material.

2.4. Polarized optical microscopy (POM)

Polarized optical microscopy (POM) is employed for the determination of spherulitic growth rates. Utilizing a Leica DMLP microscope (Leica Microsystems, Germany) equipped with an LM Plan 20x/040 lens, images are captured as a function of isothermal crystallization time.

To produce thin films, pellets are heated to 230 ℃ on a hot stage and manually compressed between two glass slides. The samples are allowed to stay at 230 ℃ for 5 minutes to relax any internal stress. Once cooled, the film is sectioned into pieces. These segments are then reheated

Table 1
Polymers investigated in this study.

Sample Code	Commercial Code	Molecular Weight			DSC 10 °C/min		
		M_w kg/mol	M_n kg/mol	Z_{eq} (M_w/M_e)	T_c °C	T_m °C	ΔHc J/g
PPH_1069K	BE50	1069	159	243	119	164	107
PPH_612K	HB311BF	612	78	139	115	162	115
PPH_540K	DM55pharm	540	92	123	112	161	115
PPH_367K	HD601CF	367	74	83	113	162	117
PPH_220K	HF420FB	220	103	50	110	159	110

between two glass discs, each with a diameter of 16 mm and a thickness of 0.15 mm. The resulting polymer film thicknesses range from 20 to 30 μm.

The POM crystallization tests followed a specific thermal protocol, applied with a Linkam THMS600 hot-stage. First, the material was heated to 230 ℃ for 5 minutes to eliminate any prior thermo-mechanical effects. Next, it was isothermally crystallized at a constant temperature (T_c) until no further crystallization changes were observed. The tested crystallization temperature ranges were 124–144 ℃ for PPH, 116–136 ℃ for PPC, and 152–160 ℃ for PPN, with intervals of 4 ℃.

2.5. *Flow-enhanced crystallization experiments*

To replicate the shear flow conditions encountered by the polymers during the 3D printing process and investigate the possibility of flow-enhanced crystallization during extrusion through the nozzle, we conducted step-shear experiments. These experiments were carried out using an HR10 rheometer (TA Instruments, USA) with 8 mm diameter parallel plates. Following an equilibration period of the melt of 3 minutes at 210 °C, a short-duration shear pulse of 3 seconds is applied at varying shear rates (20, 80, 140, and 200 s^{-1}). After the shear pulse, the sample undergoes controlled cooling at a constant rate of 5 °C/min until 80 °C. The evolution of the viscoelastic properties is measured through small amplitude oscillations (at 1% strain) at a frequency of 5 rad/s. The crystallization onset is identified by a sharp increase in viscoelastic moduli as temperature decreases. Additionally, a reference experiment without the shear pulse was conducted for comparison purposes.

2.6. *3D printing*

A pellet extruder (Direct3D, Italy), which operates on the principle of a singular extrusion head expelling molten polymer material along a three-dimensional path, was employed in this study. The extruder was mounted on an F30 (Direct 3D, Italy) 3D printer. The process begins by introducing pellets of the desired material into the inlet. A single screw then advances these pellets into the heated area, where the material undergoes melting before being extruded through the nozzle.

With this printer, we employed a layer-by-layer approach to produce walls measuring approximately 200×3x50 mm. The layer height was set to 1.5 mm, with a nozzle diameter of 2 mm and a temperature ranging from 240 °C to 210 °C. The bed was set at 60 ℃ and the printing speed was set at 7.5 mm/s. The temperature of the air around the sample is in the range of 23–25 ℃ the flow throughput is estimated as 19 mm^3/s. Predictions of the shear rate and shear stress at the nozzle wall are detailed in Section 3. Due to extensive warpage for some materials a noticeable deformation in the final product was observed.

2.7. *Infra-red imaging*

We employed thermal imaging to monitor the temperature evolution of the wall geometry during the 3D printing process, described in the previous paragraph. Real-time videos for each print were taken at a 3.75 Hz framerate via a FLIR T560 thermal camera (Teledyne FLIR LLC, USA). The camera was equipped with a Germanium lens and 24° viewing angle objective (resolution 640 × 580 pixel, measurement range 0–650 °C, accuracy ±2 °C or ±2% of reading, sensitivity <40 mK @ 30 °C).

The radiometric videos for each material-temperature combination were converted to.mp4 format through the FLIR Research Studio software, color-coding the temperature of each pixel to an appropriate linear black-to-white scale. The temperature over time curves relative to the region of interest were extracted from the videos via an appropriate in-house MatLab code.

2.8. *Tensile tests*

The printed walls were precisely shaped into specific geometries using a die cutter (Giuliani Technology, Italy). For tests perpendicular to the printing direction, rectangular specimens with a width of 10 mm and a length encompassing the full wall length were used.

Uniaxial tensile tests were performed at room temperature using an INSTRON 5569 universal testing machine (Instron, UK) equipped with a 5 kN load cell. For the measurement of the ultimate tensile strength, at least five specimens were tested for each sample and printing condition with a traction speed of 0.1 mm/s. In order to compute the exact engineering stress value, the length of the weld line was measured for each die-cut sample via a stereo-microscope [8–10]. In addition, samples of the different materials were compression moulded by heating the pellets inside two aluminium plates in a Carver press (Carver, USA) at 220 °C for 3 minutes, applying a pressure of about 45 bar. The plates were then cooled by flowing water inside the press, removed from the mould and cut in a dog-bone shape with the above-described die cutter. Finally, the samples, with thickness of about 1 mm, were tested in tensile deformation at a speed of 0.2 mm/s.

2.9. *Post-printing morphological evaluation*

Small parts of the printed wall geometry were first embedded in a resin, hardened and then cut along the midplane in a direction parallel to the printing one. Semi-thin sections of ca. 12 μm were obtained at room temperature with a Leica Nanocut R (Leica Microsystems, Germany). The sections were subsequently fixed between glass slides and imaged between crossed-polarizers with an Olympus BX51 equipped with an Olympus DP28 camera (Olympus, Japan).

3. Theoretical model

The model we employ in this work has been well established in the literature to investigate PLA [8,16], PCL [18] and PP [18] under MatEx conditions. In summary, the model considers extrusion, deposition, and cooling of a single filament.

The flow region is assumed to be isothermal and is calculated by conservation of mass coupled with an appropriate constitutive model that captures the dynamics of a linear polymer melt via a tensor equation for the polymer conformation. Importantly, the model accounts for the molecular weight of the polymer, M_w, via an entanglement number

$$Z_{eq} = \frac{M_w}{M_e} \tag{1}$$

where M_e is the molecular weight in between entanglements, which is fit to rheological characterisation. (See Appendix for further details). The assumption is that the molecular weight distribution is monodisperse, with all chains having the same length.

The modelled extrusion region corresponds to the straight, axisymmetric channel prior to the nozzle exit. Note that this section is present in the pellet-fed system used here (after the screw section), as well as typical filament-fed systems. It is assumed that there is sufficient residence time in the nozzle for the polymer to become fully molten, for all memory of prior processing to be erased, and for the polymer to reach steady state (as done in previous work [19]). For these samples under the given print conditions, the velocity profile is plug-like due to the shear-thinning nature of the polymers, with shear rates at the nozzle wall predicted to range from $\sim$ 10–100 s^{-1}, with corresponding shear stresses from 10^5 –10^6 Pa depending on the molecular weight. If the model assumptions hold, then shear rates will be similar for the same nozzle diameter and feedstock material.

Upon deposition, the flow is switched off, the polymers begin to relax back to equilibrium, and cooling of the filament commences. The boundary condition at the surface of the filament for the temperature calculation is informed by infra-red imaging measurements and takes the form

$$T_{surf} = \left(\frac{T_N - T_a}{2}\right)\exp(-t/\tau_c) + T_a \tag{2}$$

where T_N is the nozzle temperature, T_a is the build plate temperature, and $1/\tau_c$ is the cooling rate fitted to the infra-red imaging measurements, as done in previous works [8–10].

Crystallization kinetics are implemented using the Schneider rate equations for the total number, size, surface area, and volume fraction of spherulites. That is,

$$\begin{aligned} \dot{\phi}_3 &= 8\pi\dot{N}(T,\Lambda), \quad && (\phi_3 = 8\pi N_{tot}),\\ \dot{\phi}_2 &= G(T)\phi_{3,} && (\phi_2 = R_{\mathrm{tot}}),\\ \dot{\phi}_1 &= G(T)\phi_2, && (\phi_1 = S_{tot}),\\ \dot{\phi}_0 &= G(T)\phi_1, && (\phi_0 = V_{tot}), \end{aligned} \tag{3}$$

respectively, coupled with the Avrami equation

$$\phi_0 = -\ln\left(1 - \xi_g\right), \tag{4}$$

where $\xi_g$is the degree of space filling. The temperature dependent growth rate, $G(T)$, is fitted to the experimental measurements for each sample (see Appendix for details and [18] for a similar procedure). The nucleation rate, $\dot{N}(T,\Lambda)$, depends on both the temperature and the degree of polymer stretch, Λ, and takes the form

$$\dot{N} = \dot{N}_q\left(1 + \eta(\Lambda^4 - 1)\right) \tag{5}$$

The quiescent nucleation rate, $\dot{N}_q(T)$,is fit to the induction time data obtained via isothermal DSC experimental measurements (see Appendix for details and [20] for a similar procedure). The model fitting parameter, η, tunes the degree of flow-enhanced crystallization and will be varied in this work. The degree of polymer stretch is dynamic; the initial value is induced by the flow, and it will decrease as the filament cools according to the relaxation dynamics of the constitutive model.

Importantly, the reptation time of the polymer is influenced by the molecular weight, the temperature profile, and the crystallization kinetics. In fact, the reptation time takes the form

$$\tau_d = \tau_0\left(Z_{eq}\right)a(T)\beta\left(\xi_g\right) \tag{6}$$

where $\tau_0 \propto Z_{eq}^3$, $a(T)$ is the WLF shift factor for time-temperature superposition, and $\beta\left(\xi_g\right)$ is measured in Ref. [11]. See Appendix for further details.

An increased shear rate will increase the degree of polymer stretch and therefore increase the nucleation rate, which will lead to a higher nucleation density and smaller spherulites. However, the threshold for flow-enhanced crystallization occurring or not is independent of shear rate; it is a balance of the stretch relaxation time versus the cooling time that determines if the flow will affect the kinetics [14]. In previous work [15], flow-enhanced spherulites appear in a thin boundary layer near to the filament surface, where the thickness of the boundary is determined by thermal diffusivity. In a layered wall this region corresponds to the welds, whereas the bulk of the filament follows quiescent kinetics, as seen in other works [2,15].

4. Results

In this section, we report the results of our experimental measurements. We choose samples PPH_220K $\left(Z_{eq} = 50\right)$ and PPH_1069K $\left(Z_{eq} = 243\right)$ to highlight behaviour for the lowest and highest molecular weight samples. First, we report the spherulite morphology via polarized optical microscopy and the expectation of flow-enhanced crystallization via step-shear experiments. Second, we report the weld strength of each sample via mechanical testing. Discussion of the mechanisms underlying our observations are deferred to Section 4, where we employ the theoretical model discussed in Section 3 to analyse our results.

4.1. Polarised optical microscopy

Fig. 1 displays representative images obtained through polarized light optical microscopy for PPH_1069K $\left(Z_{eq} = 243\right)$ and PPH_220K $\left(Z_{eq} = 50\right)$, both printed under identical conditions and subsequently microtomed into thin slices. A noticeable difference in the spherulitic morphology is evident by simple visual inspection of the micrographs. Specifically, the average size of spherulites is significantly larger in the homopolymer with a lower molecular weight (see Fig. 1a and b), measuring approximately 100 μm in diameter. In contrast, PPH_1069K $\left(Z_{eq} = 243\right)$ exhibits smaller spherulites, the majority being less than 10 μm in diameter, with a few around 20 μm.

This nearly one-order-of-magnitude difference in average spherulite size directly corresponds to a variation of approximately 1000-fold in the number of nuclei, given the inverse relationship between spherulite volume and nuclei concentration [21]. The substantial increase in nuclei formation for higher molecular weight samples during the printing process can be attributed to the significant influence of flow-enhanced nucleation. Row-nucleated structures, testifying the effect of the applied flow field, are also sometime observed, especially at the inter-layer boundary (see Appendix). However, by visual inspection, it is difficult to determine if there is a spatial variation in the spherulite size with distance from the weld line.

4.2. FIC step-shear experiments

To investigate the occurrence of flow-enhanced crystallization under conditions simulating the printing process, we examined the storage modulus as a function of temperature for two representative materials (PPH_220K $\left(Z_{eq} = 50\right)$ and PPH_1069K $\left(Z_{eq} = 243\right)$) across various step-shear conditions (Fig. 2). Initially, there is a slight rise in modulus as temperature decreases in the molten state. This trend continues until a sudden and significant increase occurs, indicating the development of semi-crystalline morphologies. Therefore, the analysis of the observed trend of the storage modulus provides insights into the impact of flow on crystallization.

Notably, in the case of PPH_1069K $\left(Z_{eq} = 243\right)$ (Fig. 2b), a clear increase in the crystallization temperature becomes evident when shear rates exceeding 80 s^{-1} are applied. The temperature increase relative to quiescent conditions can be as high as 15 °C, when the material is subject to a step shear rate of 140 s^{-1}, close to the conditions encountered at the nozzle wall during the printing process (as determined by the theoretical model described in Section 3). In contrast, in the case of PPH_220K (Fig. 2a), there is no significant effect of shear on the crystallization temperature. This holds true even when subjecting the polymer to shear rates much higher than those experienced at the nozzle wall (20 s^{-1}). The same behaviour is exhibited by the other examined homopolymers, mirroring the one of PPH_220K $\left(Z_{eq} = 50\right)$.

We note that the shear rates chosen are representative of the shear at the nozzle wall and does not account for any additional shear deformation that may occur during deposition of the polymer onto the build plate. Therefore, we cannot eliminate the possibility of flow-enhanced crystallization occurring also in the lower molecular weight samples during MatEx. However, from these observations we do expect to see a strong influence of flow-enhanced crystallization when printing the higher molecular weight sample.

4.3. Mechanical testing

Fig. 3 reports the mechanical properties and fracture aspect of PPH_220K $\left(Z_{eq} = 50\right)$ and PPH_1069K $\left(Z_{eq} = 243\right)$. Two representative stress-strain curves (depicted in Fig. 3 on the left) demonstrate that the

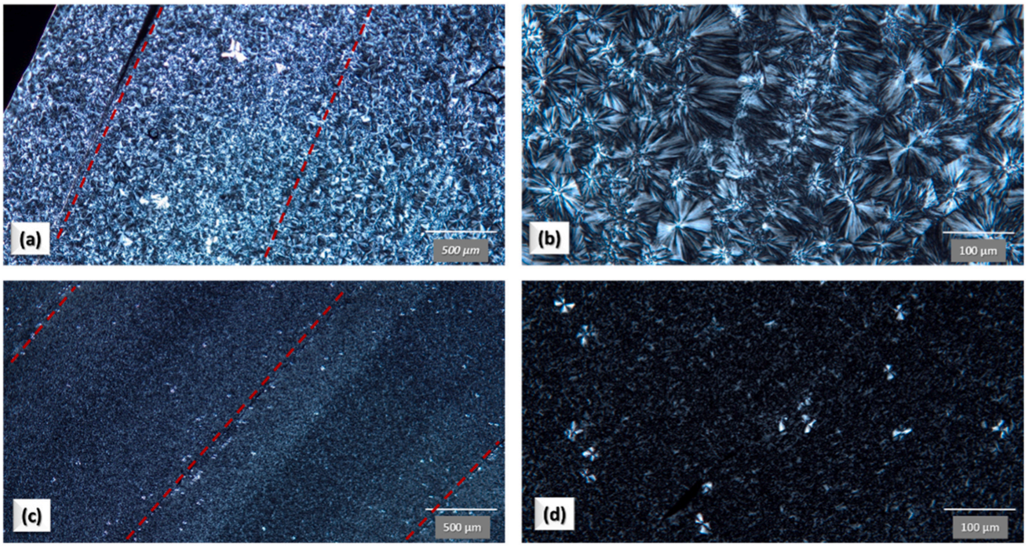

Fig. 1. Optical microscopy images at different magnification of printed specimen's cross-sections for PPH_220K $(Z_{eq} = 50)$ (a, b) and PPH_1069K $(Z_{eq} = 243)$ (c, d). Both samples were printed at a nozzle temperature of 210 °C. The dashed red lines in (a) and (c) highlight the separation between adjacent printed layers (i.e., the weld lines).

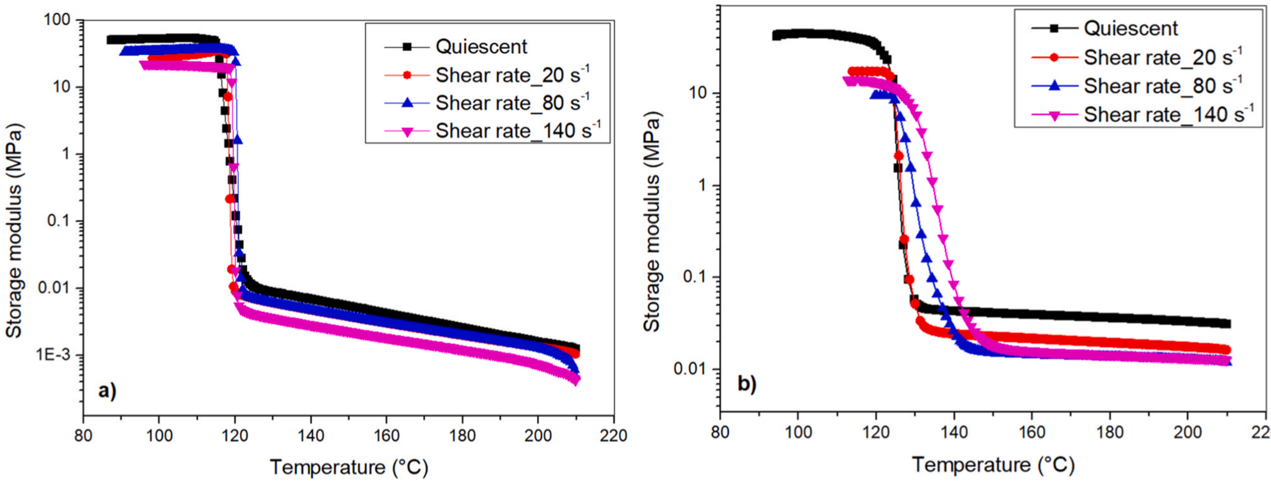

Fig. 2. Storage modulus as a function of temperature during cooling at 5 °C/min, for experiments at different shear rates applied for 3 seconds at 210 °C. (a) PPH_220K $(Z_{eq} = 50)$ and, (b) PPH_1069K $(Z_{eq} = 243)$.

highest molecular weight sample, when tested perpendicularly to the printing direction, breaks at a lower stress level compared to a sample with a lower molecular weight. Furthermore, the toughness of the specimen, calculated by the area under the stress-strain curve, is clearly less for the higher molecular weight sample.

Upon examining the fractured samples, a noticeable contrast in behaviour emerges between the two polymers with distinct molecular weights (see Fig. 3, right). Specifically, PPH_220K $(Z_{eq} = 50)$ displays a significant plastic deformation region, suggesting a weld behaviour akin to bulk material (Fig. 3, right, a and b). Conversely, PPH_1069K $(Z_{eq} = 243)$ demonstrates a brittle fracture pattern along the weld line, without any indications of plastic deformation (Fig. 3, right, c and d).

Fig. 4 shows the measured weld strength as a function of Z_{eq} for two print temperatures. We note that the weld strength of the sample PPH_1069K $(Z_{eq} = 243)$ printed at 210 °C could not be measured due to its excessive brittleness. We compare the weld strength to the yield stress of compression moulded samples of the same materials. We do not see a significant influence of the print temperature on the measured weld strength. Clearly, the weld strength is less than the yield stress of compression moulded samples for all the materials. This may be due to a combination of factors: faster cooling in MatEx resulting in a weaker crystal morphology, insufficient interdiffusion between the printed layers, residual alignment of the polymers in the weld region, and flow-enhanced crystallization effects. As such, the value of the yield stress for compression moulded sample should be considered as a reference only, rather than as representative of the fully healed strength of printed samples. Nevertheless, the dependence of weld strength on Z_{eq} suggests a significant molecular effect that goes beyond thermal protocols of MatEx versus compression moulding.

Indeed, we expect a steady decrease in weld strength with Z_{eq}; for amorphous polymers increasing molecular weight is known to decrease the amount of interdiffusion that occurs and increase the amount of residual alignment that is trapped in the weld leading to reduced strength [8]. This trend is somewhat evident in Fig. 4, although the data is quite noisy, which may be an influence of the varying crystal morphology we see in Fig. 1. Furthermore, we cannot easily identify a transition between brittle and ductile fracture, as shown in Fig. 3. We note it is difficult to draw conclusions from the mechanical data alone.

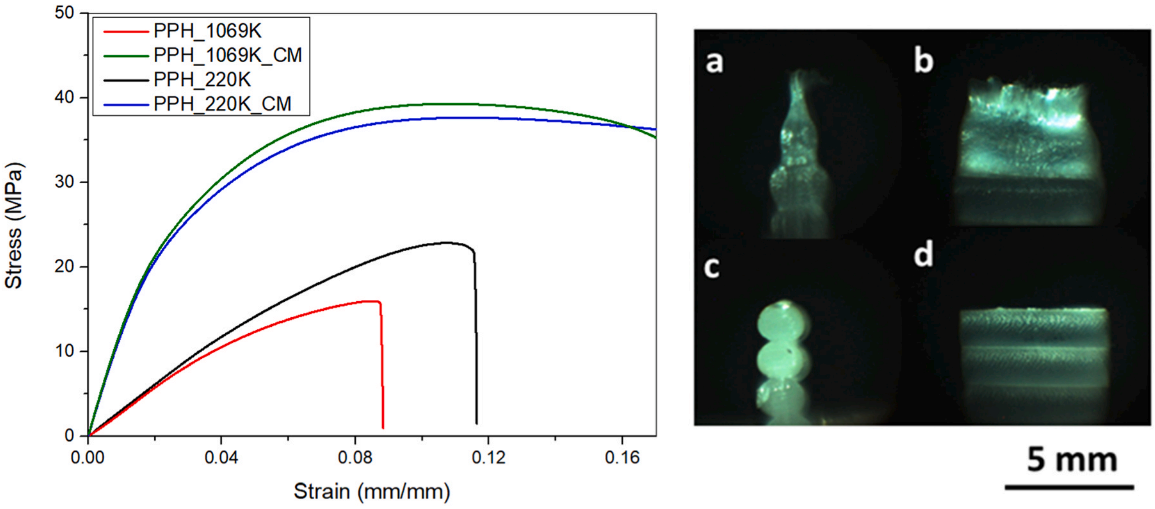

Fig. 3. Examples of stress-strain curves for both higher and lower molecular weight printed samples, compared to the curve obtained for the corresponding compression moulded sample (left); lateral and front views of the fractured specimens for PPH_220K $(Z_{eq} = 50)$ (a and b) and PPH_1069K $(Z_{eq} = 243)$ (c and d) (right). Only half of the complete fractured specimen is shown in the pictures, tensile test direction is vertical.

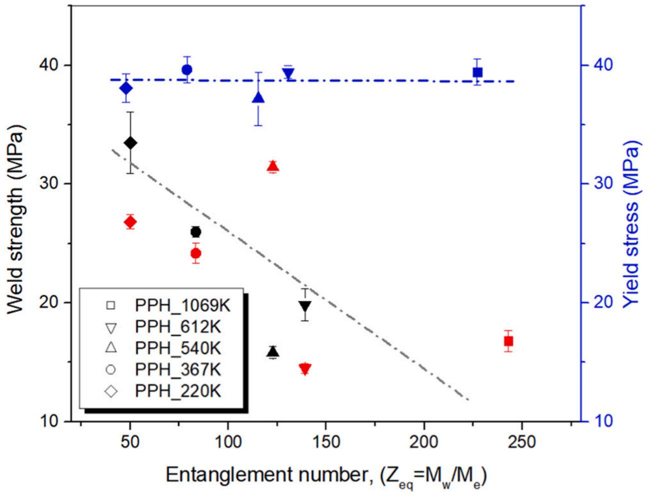

Fig. 4. Weld strength as a function of Z_{eq} for two nozzle temperatures: 210 °C (black symbols) and 240 °C (red symbols). For comparison, the yield stress of compression moulded samples of the same materials is also reported (blue symbols). The dashed lines are a guide to the eyes. Error bars represent one standard deviation.

Thus, in the next section we employ the theoretical model of Section 3 to probe microstructural effects further.

5. Discussion

By employing the theoretical model described in Section 3 that accounts for rheology and crystallization, we can predict the crystallization time and corresponding interdiffusion distance achieved under these printing conditions for each of our samples. Here we report the crystallization time, t_c, to be the time to reach full space filling $\left(\xi_g = 1\right)$. The interdiffusion distance is given by

$$\frac{\chi(t)}{R_g} \approx \left(\int_0^t \frac{1}{\tau_d(t)} dt\right)^{1/4} \qquad (7)$$

as in [22]. Since the glass transition is below room temperature for PP, interdiffusion will be arrested by the crystallization process. The amount of crystallization required to arrest diffusive molecular motion is known as “physical gelation” and has been shown to vary for different materials [23]. In this work we assume interdiffusion is arrested at t_c and report a final interdiffusion distance $\chi_c = \chi(t = t_c)$ from Eq. 7. It is expected for bulk strength of the interface to be achieved provided $\chi_c > R_g$.

Fig. 5 shows the predicted final interdiffusion distance, χ_c, for each of our samples; Fig. 5 focuses on the homopolymers, which have similar crystallization temperatures, T_c, and varying entanglement number, Z_{eq} (for samples having distinct crystallization temperatures see Appendix). By setting $\eta = 0$ we model quiescent conditions, where the crystallization process is unaffected by the polymer dynamics. We see a steady decrease in χ_c with Z_{eq} (and crystallization temperature T_c – see Appendix) with a trend similar to the mechanical testing measurements (see Fig. 4). However, under these conditions, we find that $\chi_c > R_g$ for all samples, suggesting that bulk strength should be achieved at the weld interface. Since this does not match experimental observations, we conclude there must be some other effect present. For amorphous

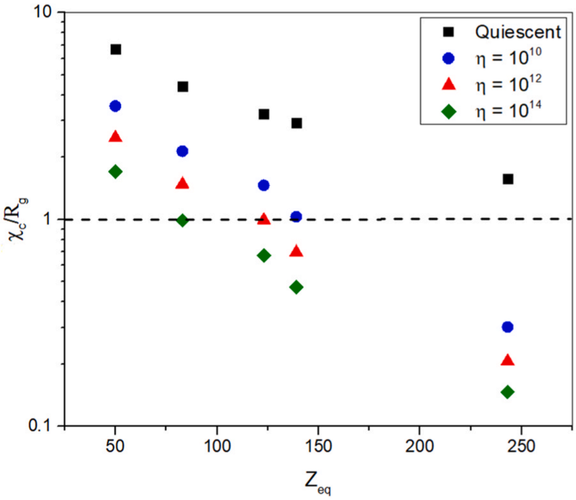

Fig. 5. Model predictions for the final interdiffusion distance, χ_c/R_g, as a function of the entanglement number Z_{eq} for homopolymers PPH_220K $(Z_{eq} = 50)$, PPH_367K $(Z_{eq} = 83)$, PPH_540K $(Z_{eq} = 123)$, PPH_612K $(Z_{eq} = 139)$, and PH_1069K $(Z_{eq} = 243)$. The model parameter η tunes the degree of flow-enhanced crystallization.

polymers this effect has been attributed to residual alignment of the polymers [8]. Here we investigate the possibility of flow-enhanced crystallization.

By setting $\eta > 0$ we can allow for flow-enhanced crystallization effects in the model. The range of η presented is similar to that explored previously in the literature (e.g., see [15]). Under these conditions, if there is residual polymer stretch at the onset of nucleation, then the nucleation rate will be accelerated. This results in a larger nucleation density, smaller spherulites to develop earlier in the cooling process, and ultimately a reduction in the time to reach full space filling, t_c. In Fig. 5, we can see that these flow effects restrict the interdiffusion process, with a reduction in χ_c with increasing η.

Fig. 6 shows the model predictions for the size of spherulites that develop in the weld region for each of the homopolymers. Under quiescent conditions, the spherulite radius is consistent across all samples and is of the order 50 μm. On the other hand, under flow conditions with $\eta = 10^{10}$ we see a marked decrease in spherulite size with entanglement number. This is a result of the larger degree of residual stretch at the onset of nucleation for higher Z_{eq}. Indeed, we note two orders of magnitude difference in the spherulite radius for PPH_220K ($Z_{eq} = 50$) and PPH_1069K ($Z_{eq} = 243$), which is qualitatively in line with the observations in Fig. 1. A comprehensive image analysis with higher resolution tools so that the spherulite radii and spatial variation can be fully resolved across all samples (such as atomic force microscopy), would be required to make a quantitative comparison of spherulite size.

Furthermore, choosing $\eta = 10^{10}$ results in $\chi_c/R_g < 1$ only for the highest molecular weight sample (see Fig. 5). While this criterion is only approximate (for example see [24]), this prediction may explain the experimental results showing a change in fracture behaviour from ductile to brittle for this sample (see Fig. 3).

We propose that it is a balance between the time to reach full space filling, t_c, and the reptation time, τ_d, that governs the welding process. From Eq. 7 we have

$$\frac{\chi_c}{R_g} \sim \left(\frac{t_c}{t_{R_g}}\right)^{1/4} \tag{8}$$

as shown in Fig. 7a, where t_{R_g} is the time taken to diffuse one radius of gyration as given by the numerical calculation of Eq. 7.

One may consider the time take to diffusion one radius of gyration to be equivalent to one reptation time. Thus, whether the threshold $\chi_c/R_g \sim 1$ is exceeded can theoretically be estimated by calculating the ratio of the crystallization time over the reptation time, t_c/τ_d. However, this estimation is non-trivial; one must have:

1. An estimate for the crystallization time, t_c. This is difficult to predict from the growth rate under non-isothermal conditions. Moreover, this time will be significantly affected by flow. Flow effects may be avoided by ensuring the polymer has sufficient time to relax before the cooling below the melting point and nucleation occurs (e.g., see [14]).
2. An estimate for the reptation time, τ_d. While the relation $\tau_d \sim 1/Z_{eq}^3$ demonstrates how molecular weight significantly limits the final interdiffusion distance (see Fig. 7b), the reptation time is very much a dynamic quantity depending on temperature and crystal fraction, as shown in Eq. 6, making a simple estimate non-trivial.

Thus, predicting t_{R_g} properly requires a numerical calculation of the integral in Eq. 7. Note that this ratio also captures the effects due to addition of nucleating agents or comonomers on the welding behaviour (see Appendix).

With a thorough characterisation of the rheological properties and crystallization kinetics under isothermal conditions, the theoretical model proposed here can be used to predict this threshold for any MatEx conditions and different polymer feedstocks. This is key for optimising the print conditions for unrestricted welding, or, on the other hand, optimising the materials characteristics such as molecular weight. As we have previously shown for amorphous materials [10], molecular weight should be considered as a key control parameter as it can be more effective in ensuring sufficient weld strength than trying to control the temperature profile.

It should be noted that the model employed here does not account for polydispersity of the samples. Polydispersity, and in particular the presence of a high-molecular weight tail in the molecular weight distribution, can enhance flow-enhanced crystallization effects further [25]. On the other hand, a low molecular weight tail can promote interdiffusion [26]. Polydispersity can be incorporated using the polySTRAND model of Read et al. [27] and will be the focus of future work. In particular, modelling the full molecular weight distribution will enable verification of the model parameter η via direct comparison with step-shear flow-enhanced crystallization experiments.

Furthermore, the model does not couple the polymer dynamics to how spherulite structures develop. For example, in Figure A4, we observe the presence of row-nucleated spherulites, which we believe to be a result of polymer chain alignment directing, as well as enhancing, crystallization. These structures will also be enhanced for samples with broad polydispersity.

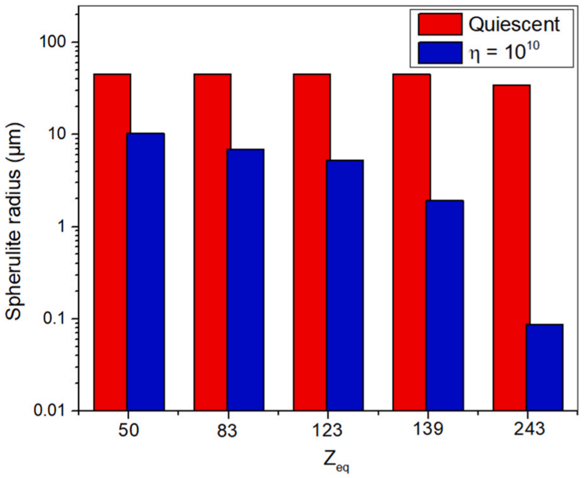

Fig. 6. Model prediction for the spherulite radius that develops in the weld region as a function of entanglement number Z_{eq} for each homopolymer (PPH_220K ($Z_{eq} = 50$), PPH_367K ($Z_{eq} = 83$), PPH_540K ($Z_{eq} = 123$), PPH_612K ($Z_{eq} = 139$), and PH_1069K ($Z_{eq} = 243$)).

6. Conclusion

In this paper we investigate various grades of polypropylene feedstock for MatEx printing, analysing the effect that both molecular weight and the crystallization kinetics have on the welding behaviour at the interfaces between layers in the z-direction. As is typically observed across all feedstock materials, the mechanical strength at the weld is significantly lower than the yield stress of the polymer, as measured by compression moulding. Additionally, we observe plastic deformation versus brittle fracture depending on the molecular weight of the feedstock, as well as spherulitic structures in the weld region that have markedly different length scales. Step-shear crystallization experiments suggest that flow-enhanced crystallization will have significant effects for higher molecular weight samples under typical print conditions.

To understand this behaviour, we employ a theoretical model that has been well tested in the literature. Selection of the model parameters requires comprehensive characterisation of the rheology and the crystallization kinetics, as well as infra-red imaging measurements to verify the cooling profile. The interdiffusion distance is predicted via the

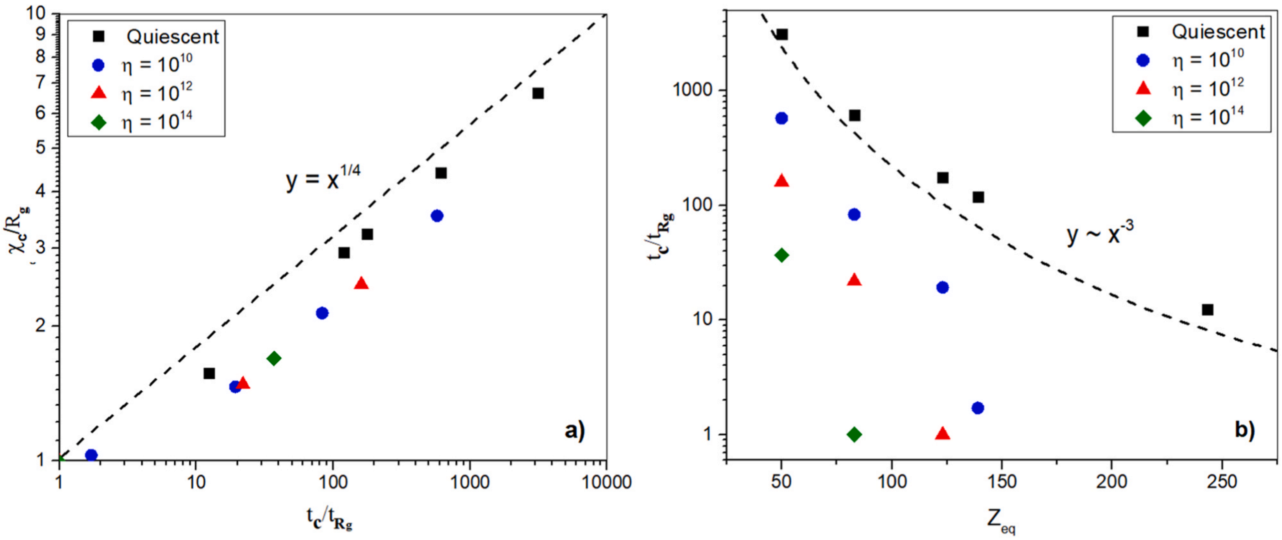

Fig. 7. (a) Model prediction for χ_c/R_g as a function of the ratio t_c/t_{R_g}, where t_{R_g} is the time taken to diffuse one radius of gyration, i.e., the equivalent to one reptation time. The model parameter η tunes the degree of flow-enhanced crystallization. The five quiescent data points correspond to the five homopolymer samples. For $\eta > 0$, not all samples achieve the threshold $\chi_c/R_g \sim 1$ so these points are null. (b) Ratio t_c/t_{R_g} as a function on entanglement number, Z_{eq}.

polymer reptation time that accounts for molecular weight, the decreasing temperature, and the onset of crystallization that arrests diffusion of the polymer. Weld strength is therefore expected to increase in samples that have a longer crystallization time, t_c.

In trends similar to the mechanical testing data, we find that the degree of interdiffusion decreases with molecular weight (and the crystallization temperature) due to the decreased time available for welding. The model suggests that welding may be further restricted by a flow-enhanced crystallization mechanism; residual polymer stretch accelerates the nucleation rate leading to a larger nucleation density, which causes smaller spherulites to develop earlier in the cooling process. The decreased crystallization time may lead to $\chi_c/R_g < 1$, which we propose to be the reason for a change in fracture pattern observed experimentally. Furthermore, only by accounting for flow-enhanced crystallization do we predict reductions by an order of magnitude in the spherulite diameter as molecular weight is increased, as observed via polarized optical microscopy.

Thus, we present first time evidence that flow-enhanced crystallization during MatEx can impact the spherulitic structure in the weld. This may impede the welding dynamics and lead to significantly reduced mechanical strength at the weld. Future work will investigate the interplay between the polymer dynamics and spherulite development as a mechanism for oriented crystallization, with the formation of row-nucleated structures. There is also scope to investigate how robust the modelling approach is to different systems; in particular the initial condition imposed by the nozzle flow assumes both the polymer deformation and the temperature reaches steady state, which can potentially break down depending on the nozzle geometry and the molecular weight of the feedstock. Questions also arise on how the welding behaviour depends on the deposition time between each layer, which depends on both the print speed and print geometry.

CRediT authorship contribution statement

Dario CAVALLO: Writing – review & editing, Supervision, Methodology, Funding acquisition, Conceptualization. **Andrea Lanfranchi:** Writing – review & editing, Investigation. **Andrea Costanzo:** Writing – review & editing, Investigation. **Jessy Koster:** Writing – review & editing, Investigation, Data curation. **Riccardo Vezzoli:** Writing – review & editing, Investigation. **Zakarya Baouch:** Writing – original draft, Investigation, Formal analysis. **Claire McIlroy:** Writing – original draft, Validation, Software, Methodology, Formal analysis, Conceptualization.

Declaration of Competing Interest

The authors declare the following financial interests/personal relationships which may be considered as potential competing interests: Dario Cavallo reports financial support was provided by European Union. If there are other authors, they declare that they have no known competing financial interests or personal relationships that could have appeared to influence the work reported in this paper

Data availability

Data will be made available on request.

Acknowledgements

Davide Tranchida and Klaus Buchmann from Borealis Polyolefine Gmbh are gratefully acknowledged for carrying out the microtoming and POM characterization of the post-printed samples. D.C. and Z.B. acknowledge funding from the European Union (Next-Generation EU), through the University of Genoa (Curiosity-driven 2021 project); D.C. also acknowledges support by the University of Genoa through the call D.R n. 3384 of 26/07/2021 funded by European Union – Next-Generation EU.

Appendix

In this Appendix, we also compare the results of the polypropylene homopolymer to a random poly(propene-co-ethylene) copolymer (PPC), and a polypropylene homopolymer with the addition of a nucleating agent (PPN). These samples are also sourced from Borealis Polyolefine GmbH. The main characteristics are given in Table A1. Note that the nucleating agent is proprietary; the commercial code is given in Table A1.

Table A1
Polymers investigated in the Appendix

Sample Code	**Commercial Code**	**Molecular Weight**				**DSC 10 °C/min**		
		Ethylene content mol%	M_W kg/mol	M_n kg/mol	Z_{eq} (M_w/M_n)	T_c °C	T_m °C	ΔHc J/g
PPH_367K	HD601CF	0	367	74	83	113	162	117
PPC_342K	RD204CF	3.4	342	107	78	105	147	95
PPH_220K	HF420FB	0	220	103	50	110	159	110
PPN_206K	HF955MO	0	206	28	47	130	171	123

Material Characterisation

Characterization of the rheology and crystallization kinetics provide the key parameters for the model. Fig. A1 shows, for all the investigated samples, the characteristic pseudoplastic behaviour observed in polymer melts. This is characterized by an initial viscosity plateau at low shear rates, followed by a decreasing trend of the viscosity that conforms to a power law relationship with the deformation rate.

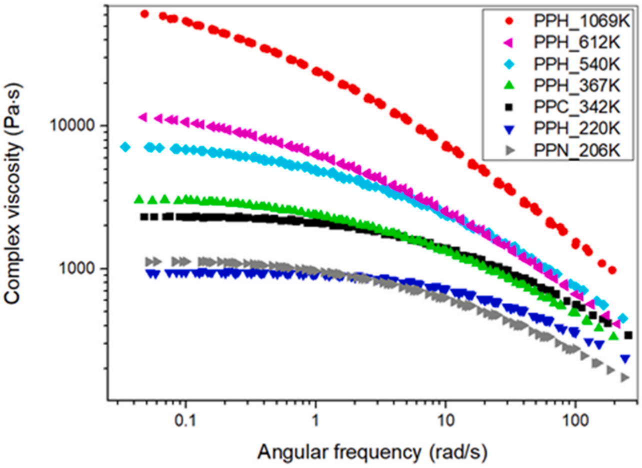

Fig. A1. Complex viscosity as a function of angular frequency for the different PP samples.

The relationship between molecular weight and complex viscosity is evident from the data. In fact, as the molecular weight increases from 220 kg/mol to 1069 kg/mol, the Newtonian viscosity escalates significantly, moving from 1000 Pa·s to over 60000 Pa·s.

Notably, the inclusion of a co-monomer in the polymer structure has no impact on viscosity, as the latter is primarily determined by the molecular weight. This enables the comparison of samples with similar rheological properties but varying levels of crystallizability (PPH_367K, PPC_342K, and PPN_206K).

As discussed in the main text, the key to the modelling approach is the definition of the reptation time

$$\tau_d = \tau_0\left(Z_{eq}\right)a(T)\beta\left(\xi_g\right) \tag{A1}$$

which depends on molecular weight, temperature, and crystallinity. The molecular weight and temperature dependence relies on appropriate materials characterisation, whereas the dependence on crystallization is empirical.

The rheological master curve is constructed by time-temperature superposition, where the shift factors are calculated according to

$$a(T) = \exp\left(\frac{-C_1(T - T_0)}{C_2 + T - T_0}\right) \tag{A2}$$

with constants $C_1 = 33.6, C_2 = 1269, T_0 = 210^{\circ}\mathrm{C}$. This gives the temperature dependence of the reptation time. The master curve of the viscoelastic moduli (not shown) also provides the entanglement molecular weight $M_e = 4.4$ kg/mol and the entanglement time of a single entanglement segment $\tau_e(T_0) = 1.7 \times 10^{-8}$ s at the reference temperature T_0 using RepTate software; these values are aligned with literature values, as discussed previously [18]. The reptation time at the reference temperature is given by

$$\tau_0\left(Z_{eq}\right) = 3\tau_e Z_{eq}^3\left(1 - \frac{3.38}{\sqrt{Z_{eq}}} + \frac{4.17}{Z_{eq}} - \frac{1.55}{Z_{eq}^{3/2}}\right) \tag{A3}$$

which gives the molecular weight dependence. These rheological parameters are consistent across all PP samples. The samples do differ however in their crystallization kinetics.

Fig. A2 compiles the spherulitic growth rate data plotted against temperature for all the examined materials. Generally, a significant reduction in growth rate is observed as temperature rises across all polymers. Specifically, the growth rates decelerate by more than two orders of magnitude with a decrease in undercooling of approximately 20 °C. Notably, all the homopolymers, including the nucleated variant, exhibit similar growth rates. Nonetheless, this uniform growth rate does not imply identical overall crystallization kinetics, as the quantity of nucleation in quiescent conditions may vary from one sample to another.

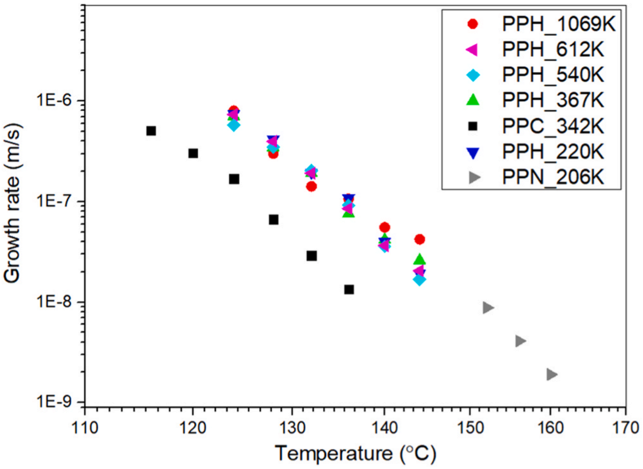

Fig A2. Growth rate as a function of temperature for the various samples.

The introduction of ethylene as a co-monomer in the polymer structure leads to a significant reduction in the crystal growth rate, as the co-units introduce defects in the crystallization process. To achieve growth rates like those of the homopolymer, the undercooling of PPC_342K must be increased by approximately 8 °C.

In the model, the growth rate takes the form

$$G(T) = G_{\max}\exp\left(-\frac{U}{T - T_{\inf}}\right)\exp\left(-\frac{K_g(T - T_m)}{2T^2(T_m - T)}\right) \tag{A5}$$

where $T_m = 194°\mathrm{C}$, $T_{\inf} = -37.2°\mathrm{C}$, and $U = 751.6°\mathrm{C}$. The parameters $G_{\max}$ and K_g are then fit to each sample independently.

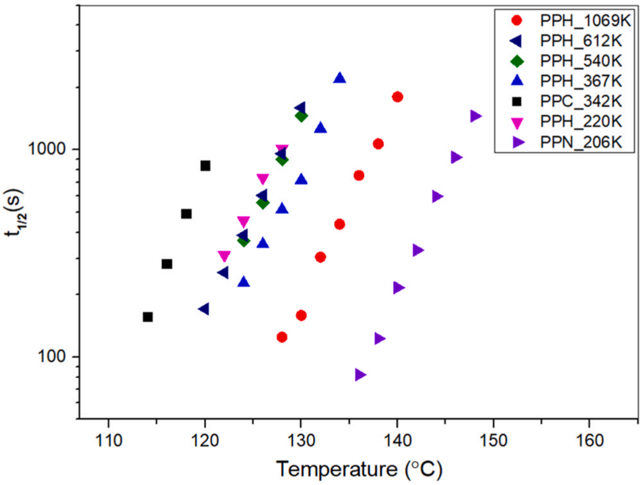

Fig A3. Half-crystallization time as a function of temperature, as measured via isothermal DSC, for the various samples.

Figure A3 presents the relationship between the crystallization temperature and the half-crystallization times of the samples under analysis, obtained via DSC. These times serve as an indicator of the overall crystallization rate, including contributions from both the crystal nucleation and growth stages. As expected, the half-crystallization time increases with increasing crystallization temperatures for all the examined polymers. Notably, nucleated polypropylene exhibits significantly accelerated crystallization kinetics, enabling measurable rates of crystallization even at higher temperatures compared to the other samples. Given that the growth rate of this polymer is comparable to the one of the other homopolymers, as demonstrated in Figure A2, the acceleration in the overall crystallization rate is attributed to the influence of the nucleating agent. Conversely, the random propene/ethylene copolymer exhibits a comparatively slower overall crystallization kinetics compared to the homopolymers, aligning with its lower growth rate, as depicted in Figure A2. Finally, the homopolymers with varying molecular weights all exhibit similar crystallization half-times, except for PPH_1069K, which crystallizes more rapidly than the others. Given that we have demonstrated that the growth rate is not influenced by molecular weight (as illustrated in Figure A2), the accelerated crystallization rate observed in the highest molecular weight sample can be attributed to a greater nucleation rate in comparison to the other pure homopolymers.

The quiescent nucleation rate takes the form

$$\dot{N}_q(T) = N_0 \exp\left(-\frac{U}{T-T_{\inf}}\right)\exp\left(-\frac{K_n T_m^4}{(T_m-T)^2}\right) \tag{A6}$$

Here the parameters N_0 and K_n are adjusted so that quiescent nucleation rate gives the measured half-crystallization time. The growth rate and nucleation rate are employed in the Schneider rate equations to calculate how the degree of space filling develops over time.

Finally, the reptation time is found to depend on the degree of space filling according to the function

$$\beta(\xi_g) = 1 - \frac{1}{0.055+\exp(6.1)} + \frac{1}{\left(0.055+\exp\left(-397\xi_g+6.1\right)\right)} \tag{A7}$$

by fitting the data given in Figure 10 of Ref. [11]. We note that this a specific to a single grade of polypropylene and the measurement is taken during isothermal crystallization. There is considerable variation for different crystallization temperatures that we do not account for here.

Row-nucleated structures

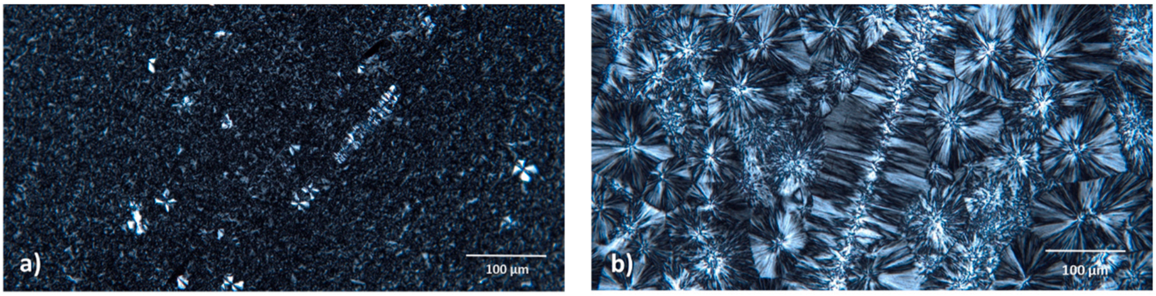

Fig A4. Optical microscopy images of printed specimen's cross-sections for PPH_1069K (a) and PPH_220K (b). Both simples were printed at a nozzle temperature of 210 °C.

The optical microscopy images displayed in Fig. A4 evidence, other than the difference in nucleation density between the two materials of different molecular weight, as already highlighted in the main text (Figure 1new) and captured by the model (Fig. 7), the presence of some row-nucleated structures, which derive from mildly oriented polymer chains.

Nucleating Agents and Co-Polymers

It is clear from the crystallization kinetics that addition of either a nucleating agent or a co-monomer will change the crystallization time, t_c. In Fig. A5 and Fig. A6, we show how this affects the properties of the weld. Figure A5 shows the weld strength as a function of the crystallization temperature, T_c, for two different print temperatures; as with the homopolymers there is scatter in the data, but overall, there is a decrease in strength with crystallization temperature. We attribute this to a decreased crystallization time decreasing the degree of interdiffusion that occurs before t_C, as shown in Figure A6. In the case of flow-enhanced crystallization, the nucleated PPN_206K ($T_c = 130$ °C) falls short of the threshold $\chi_c/R_g \sim 1$ for the range of η investigated. In contrast the co-polymer PPC_342K ($T_c = 105$ °C) remains close to quiescent conditions. We find that this behaviour also collapses to $\chi_c/R_g \sim t_c/t_{R_g}$ as shown in Fig. A7, demonstrating that our theoretical model also captures the effect of changes to the crystallization temperature via additives.

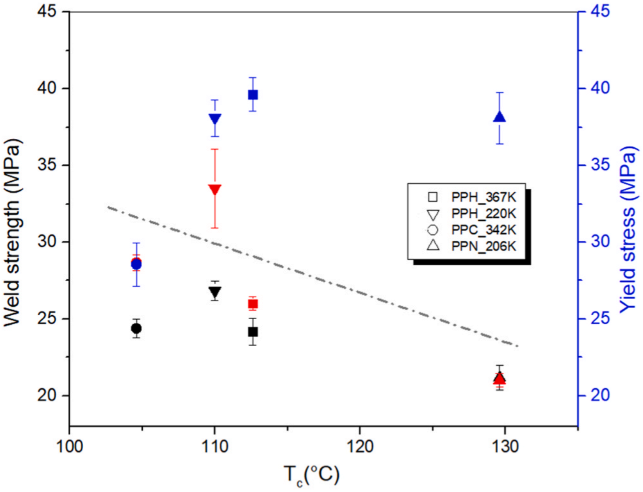

Fig A5. Weld strength as a function of T_c at nozzle temperature of 210 °C (black symbols) and 240 °C (red symbols). For the sake of comparison, the yield stress of compression moulded samples of the same materials is also reported (blue symbols). The dashed line is a guide to the eyes.

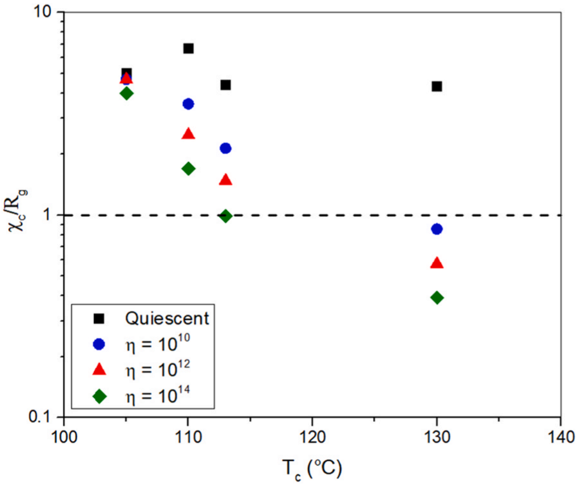

Fig A6. Model predictions for the final interdiffusion distance, χ_c/R_g, as a function the crystallization temperature T_c for samples PPC_342K $(Z_{eq} = 78)$, PPN_206K $(Z_{eq} = 47)$, PPH_367K $(Z_{eq} = 83)$, and PPH_220K $(Z_{eq} = 50)$. The model parameter η tunes the degree of flow-enhanced crystallization.

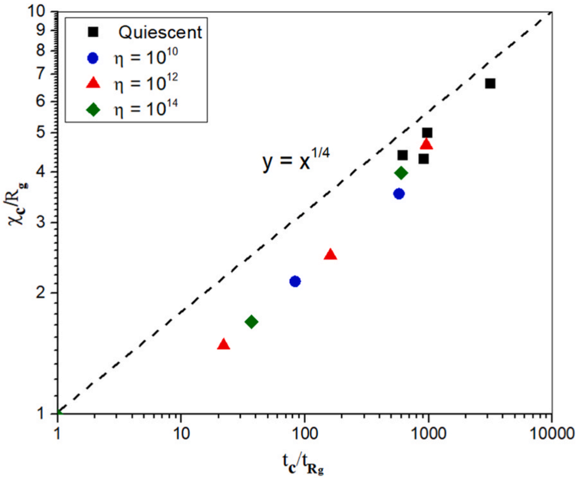

Fig A7. Model prediction for χ_c/R_g as a function of the ratio t_c/t_{R_g}, where t_{R_g} is the time taken to diffuse one radius of gyration, i.e., the equivalent to one reptation time. The model parameter tunes the degree of flow-enhanced crystallization. The four quiescent data points correspond to samples PPC_342K $(Z_{eq} = 78)$, PPN_206 $(Z_{eq} = 47)$, PPH_367K $(Z_{eq} = 83)$, and PPH_220K $(Z_{eq} = 50)$. For $\eta > 1$ not all samples achieve the threshold $\chi_c/R_g \sim 1$, so these points are null.

References

[1] A. Das, C. McIlroy, M.J. Bortner, Advances in modeling transport phenomena in material-extrusion additive manufacturing: coupling momentum, heat, and mass transfer, Prog. Addit. Manuf. 6 (2021) 3–17, https://doi.org/10.1007/s40964-020-00137-3.

[2] S. Hertle, M. Drexler, D. Drummer, Additive manufacturing of poly(propylene) by means of melt extrusion, Macromol. Mater. Eng. 301 (2016) 1482–1493, https://doi.org/10.1002/mame.201600259.

[3] M. Jin, R. Giesa, C. Neuber, H.W. Schmidt, Filament materials screening for FDM 3D printing by means of injection-molded short rods, Macromol. Mater. Eng. 303 (2018) 1–7, https://doi.org/10.1002/mame.201800507.

[4] M. Spoerk, C. Holzer, J. Gonzalez-Gutierrez, Material extrusion-based additive manufacturing of polypropylene: a review on how to improve dimensional inaccuracy and warpage, J. Appl. Polym. Sci. 137 (2020) 1–16, https://doi.org/10.1002/app.48545.

[5] S. Petersmann, P. Spoerk-Erdely, M. Feuchter, T. Wieme, F. Arbeiter, M. Spoerk, Process-induced morphological features in material extrusion-based additive manufacturing of polypropylene, Addit. Manuf. 35 (2020) 101384, https://doi.org/10.1016/j.addma.2020.101384.

[6] M. Huang, Y. Xu, A.K. Schlarb, Mechanical performance and supermolecular morphology of void free polypropylene manufactured by fused filament fabrication, J. Appl. Polym. Sci. 138 (2021) 1–11, https://doi.org/10.1002/app.51409.

[7] J.E. Seppala, S. Hoon Han, K.E. Hillgartner, C.S. Davis, K.B. Migler, Weld formation during material extrusion additive manufacturing, Soft Matter 13 (2017) 6761–6769, https://doi.org/10.1039/c7sm00950j.

[8] A. Costanzo, R. Spotorno, M.V. Candal, M.M. Fernández, A.J. Müller, R.S. Graham, D. Cavallo, C. McIlroy, Residual alignment and its effect on weld strength in material-extrusion 3D-printing of polylactic acid, Addit. Manuf. 36 (2020) 101415, https://doi.org/10.1016/j.addma.2020.101415.

[9] A. Costanzo, D. Cavallo, C. McIlroy, High-performance co-polyesters for material-extrusion 3D printing: A molecular perspective of weld properties, Addit. Manuf. 49 (2022) 102474, https://doi.org/10.1016/j.addma.2021.102474.

[10] A. Costanzo, A. Poggi, S. Looijmans, D. Venkatraman, D. Sawyer, L. Puskar, C. Mcllroy, D. Cavallo, 2022, The Role of Molar Mass in Achieving Isotropy and Inter-Layer Strength in Mat-Ex Printed Polylactic Acid.

[11] R. Pantani, V. Speranza, G. Titomanlio, Evolution of iPP relaxation spectrum during crystallization, Macromol. Theory Simul. 23 (2014) 300–306, https://doi.org/10.1002/mats.201300147.

[12] D.W. Collinson, N. Von Windheim, K. Gall, L.C. Brinson, Direct evidence of interfacial crystallization preventing weld formation during fused filament fabrication of poly (ether ether ketone, Addit. Manuf. 51 (2022) 102604, https://doi.org/10.1016/j.addma.2022.102604.

[13] E.L. Gilmer, D. Anderegg, J.M. Gardner, G. Sauti, E.J. Siochi, S.H. Mcknight, D. A. Dillard, C. Mcilroy, M.J. Bortner, Temperature, diffusion, and stress modeling in filament extrusion additive manufacturing of polyetherimide: an examination of the influence of processing parameters and importance of modeling assumptions, Addit. Manuf. 48 (2021) 102412, https://doi.org/10.1016/j.addma.2021.102412.

[14] C. McIlroy, A fundamental rule: determining the importance of flow prior to polymer crystallization, Phys. Fluids 31 (2019), https://doi.org/10.1063/1.5129119.

[15] C. McIlroy, R.S. Graham, Modelling flow-enhanced crystallisation during fused filament fabrication of semi-crystalline polymer melts, Addit. Manuf. 24 (2018) 323–340, https://doi.org/10.1016/j.addma.2018.10.018.

[16] C. McIlroy, J.E. Seppala, A.P. Kotula, Combining modeling and measurements to predict crystal morphology in material extrusion, ACS Symp. Ser. 1315 (2019) 85–113, https://doi.org/10.1021/bk-2019-1315.ch006.

[17] R. Pantani, I. Coccorullo, V. Speranza, G. Titomanlio, Modeling of morphology evolution in the injection molding process of thermoplastic polymers, Prog. Polym. Sci. 30 (2005) 1185–1222, https://doi.org/10.1016/j.progpolymsci.2005.09.001.

[18] A. Das, J.A. Riet, M.J. Bortner, C. McIlroy, Rheology, crystallization, and process conditions: The effect on interlayer properties in three-dimensional printing, Phys. Fluids 34 (2022), https://doi.org/10.1063/5.0128660.

[19] C. McIlroy, P.D. Olmsted, Deformation of an amorphous polymer during the fused-filament-fabrication method for additive manufacturing, J. Rheol. 61 (2017) 379–397, https://doi.org/10.1122/1.4976839.

[20] J. Pu, C. McIlroy, A. Jones, I. Ashcroft, Understanding mechanical properties in fused filament fabrication of polyether ether ketone, Addit. Manuf. 37 (2021) 101673, https://doi.org/10.1016/j.addma.2020.101673.

[21] J. Molnár, Ö. Sepsi, G. Erdei, S. Lenk, F. Ujhelyi, A. Menyhárd, Modeling of light scattering and haze in semicrystalline polymers, J. Polym. Sci. 58 (2020) 1787–1795, https://doi.org/10.1002/pol.20200027.

[22] C. McIlroy, P.D. Olmsted, Disentanglement effects on welding behaviour of polymer melts during the fused-filament-fabrication method for additive manufacturing, Polymer 123 (2017) 376–391, https://doi.org/10.1016/j.polymer.2017.06.051.

[23] C.A. Chatham, M.J. Bortner, B.N. Johnson, T.E. Long, C.B. Williams, Predicting mechanical property plateau in laser polymer powder bed fusion additive manufacturing via the critical coalescence ratio, Mater. Des. 201 (2021) 109474, https://doi.org/10.1016/j.matdes.2021.109474.

[24] T. Ge, F. Pierce, D. Perahia, G.S. Grest, M.O. Robbins, Molecular dynamics simulations of polymer welding: Strength from interfacial entanglements, Phys. Rev. Lett. 110 (2013) 1–5, https://doi.org/10.1103/PhysRevLett.110.098301.

[25] D.W. Thurman, M. Seki, J.P. Oberhauser, J.A. Kornfield, Shear-mediated crystallization of isotactic polypropylene: The role of long chain-long chain overlap, Am. Chem. Soc. Polym Prepr. Div. Polym. Chem. 43 (2002) 315–316.

[26] N.P. Levenhagen, M.D. Dadmun, Bimodal molecular weight samples improve the isotropy of 3D printed polymeric samples, Polymer 122 (2017) 232–241, https://doi.org/10.1016/j.polymer.2017.06.057.

[27] D.J. Read, C. McIlroy, C. Das, O.G. Harlen, R.S. Graham, PolySTRAND model of flow-induced nucleation in polymers, Phys. Rev. Lett. 124 (2020) 147802, https://doi.org/10.1103/PhysRevLett.124.147802.